Extremely large oscillations of cantilevers subject to motion constraints

Hamed Farokhi [a], Mergen H. Ghayesh [b,*]

[a] *Department of Mechanical and Construction Engineering, Northumbria University, Newcastle upon Tyne NE1 8ST, UK*
[b] *School of Mechanical Engineering, University of Adelaide, South Australia 5005, Australia*
**Corresponding author: mergen.ghayesh@adelaide.edu.au*
Email: (H Farokhi): hamed.farokhi@northumbria.ac.uk

Abstract

The nonlinear extremely large-amplitude oscillation of a cantilever subject to motion constraints is examined for the first time. In order to be able to model the large-amplitude oscillations accurately, the equation governing the cantilever centreline rotation is derived. This allows for analysing motions of very large amplitude even when tip angle is larger than $\pi/2$. The Euler-Bernoulli beam theory is employed along with the centreline inextensibility assumption, which results in nonlinear inertial terms in the equation of motion. The motion constraint is modelled as a spring with a large stiffness coefficient. The presence of a gap between the motion constraint and the cantilever causes major difficulties in modelling and numerical simulations, and results in a non-smooth resonance response. The final form of the equation of motion is discretised via the Galerkin technique, while keeping the trigonometric functions intact to ensure accurate results even at large-amplitude oscillations. Numerical simulations are conducted via a continuation technique, examining the effect of various system parameters. It is shown that the presence of the motion constraints widens the resonance frequency band effectively which is particularly important for energy harvesting applications.

Keywords: Cantilever; Motion constraint; Extremely large-amplitude oscillation; Nonlinear damping; Bistability

1. Introduction

Temporary contact and impact between components are present in many mechanical structures and machines, such as piping systems, vibration isolators, gears with clearances, and impact damping elements. Impact between components is also present in a specific class of energy harvesters [1, 2]. For all these systems, accurate modelling and analysis of the dynamical behaviour of the system is essential for predicting the motion amplitudes as well as the developed force and stress magnitudes, to ensure smooth operation and prevent improper functioning and immature failure of system components.

The early studies on this topic focused on investigating the behaviour of piece-wise linear discrete systems [3-10]. For instance, Moon and Shaw [3] studied the chaotic vibrations of an elastic beam with nonlinear boundary conditions. Nigm and Shabana [11] conducted a theoretical analysis on the steady-state vibrational characteristics of a discrete system subject to an impact damper. Further investigation was conducted by Shaw and Holmes [4], who studied vibrational behaviour of a single degree-of-freedom (DOF) piecewise linear oscillator. Choi and Noah [5] examined the forced response of a single DOF system involving an unsymmetrical piecewise linear stiffness using a harmonic balance technique together with the fast Fourier transformation. The investigations were continued by Natsiavas [9], who examined the dynamics of oscillators with bi-linear damping and stiffness. There are also a few studies

examining some aspects of the dynamics of constrained continuous systems [12, 13]. For instance, Metallidis and Natsiavas [14] examined the axial vibration response of a periodically excited deformable rod subject to motion-limiting constraint. Björkenstam [12] studied the motion and dynamic stability of a bar subjected to a periodic driving force, a linear damping force and impact forces due to its motion.

Most of the recent studies on this topic focus on the application of motion constraints in enhancing the efficiency of vibration-based energy harvesters via widening the resonance frequency band. For instance Liu et al. [15] used a lumped model to analyse the response of a piezoelectric energy harvester subject to motion constraints. Soliman et al. [16] developed an energy harvester design implementing motion constraints to widen the frequency band. Similar theoretical and experimental investigations have been performed on design and analysis of vibration-based energy harvesters by, for instance, Halim and Park [17], Wu et al. [18], and Liu et al. [1]. All of these valuable studies are based on experimental observations and/or discrete (lumped mass) theoretical analysis.

The present study, for the first time, investigates the nonlinear extremely large-amplitude oscillation of a cantilever under base excitation subject to motion-limiting constraints from both sides, employing a *continuous model*. In particular, a continuous model of the cantilever is developed on the basis of the Euler-Bernoulli beam theory and inextensibility condition. The centreline rotation is considered as the main variable describing the motion of the cantilever; this allows analysing very large-amplitude motions accurately. The effect of the motion constraint is accounted for via a spring with a clearance. The presence of an initial gap

(clearance) between the cantilever and the motion constraint causes major challenges in continuous modelling and numerical simulations. The continuous model is discretised employing the Galerkin technique and solved using a continuation technique. Numerical results are presented in the form of frequency-amplitude diagrams, time histories, and phase-plane portraits.

2. Model development

The system under consideration, as shown in Fig. 1, is a cantilever under base excitation subjected to motion constraints. The motion of the cantilever is analysed in a Cartesian coordinate system with x and z denoting the axial and transverse directions. The cantilever is of length L, width b, and thickness h. The motion constraints are located at a distance x_c from the base, with a gap width of g_0 from each side; both motion constraints have the same stiffness. The whole cantilever system is under harmonic base excitation of amplitude w_0 and frequency ω.

One of the well-known assumptions in modelling of cantilevers is the inextensibility of the centreline. Under this assumption, the longitudinal displacement, $u(x,t)$, and the transverse displacement (with respect to the base), $w(x,t)$, can be written as a function of the rotation angle of the centreline, $\theta(x,t)$, as

$$u(x,t)=\int_0^x\left(\cos\left[\theta(x,t)\right]-1\right)\mathrm{d}x,$$
$$w(x,t)=\int_0^x\sin\left[\theta(x,t)\right]\mathrm{d}x. \tag{1}$$

The total transverse displacement, $w_t(x,t)$, is given by

$$w_t(x,t)=w(x,t)+w_0\sin\left(\omega t\right)=\int_0^x\sin\left[\theta(x,t)\right]\mathrm{d}x+w_0\sin\left(\omega t\right). \tag{2}$$

The relations in Eq. (1) allows for deriving the rotational equation of motion of the cantilever. The advantage of the rotational equation of motion over the transverse equation of motion is that it is capable of predicting very-large-amplitude oscillations even when the tip angle is larger than $\pi/2$. In what follows, the kinetic and potential energies as well as the work of damping are obtained in terms of the rotation angle.

The axial strain of the cantilever under inextensibility assumption can be formulated as [19]

$$\varepsilon=-z\frac{\partial\theta(x,t)}{\partial x}. \tag{3}$$

Based on the Kelvin-Voigt energy dissipation mechanism, the axial stress can be expressed as

$$\sigma=\underset{\sigma_e}{E\varepsilon}+\underset{\sigma_v}{\eta\frac{\partial\varepsilon}{\partial t}} \tag{4}$$

where E and η stand for Young's modulus and material viscosity; σ_e and σ_v respectively denote the elastic and viscous components of the axial stress.

The strain energy of the cantilever is given by [20]

$$\Pi = \frac{1}{2}\int_V \sigma_e \varepsilon \, \mathrm{d}V = \frac{1}{2} EI \int_0^L \left(\frac{\partial \theta(x,t)}{\partial x} \right)^2 \mathrm{d}x. \tag{5}$$

in I represents the second moment of area.

The virtual work done by the viscous component of the axial stress can be formulated as

$$\delta W_v = -\int_V \sigma_v \delta\varepsilon \, \mathrm{d}V = -\eta I \int_0^L \left[\frac{\partial^2 \theta(x,t)}{\partial x \partial t} \delta \left(\frac{\partial \theta(x,t)}{\partial x} \right) \right] \mathrm{d}x. \tag{6}$$

The kinetic energy of the cantilever under base-excitation can be obtained as

$$\begin{aligned} KE = {} & \frac{1}{2}\rho I \int_0^L \left(\frac{\partial \theta(x,t)}{\partial t} \right)^2 \mathrm{d}x + \frac{1}{2}\rho A \int_0^L \left(\int_0^x \frac{\partial \theta(x,t)}{\partial t} \sin\left[\theta(x,t)\right] \mathrm{d}x \right)^2 \mathrm{d}x \\ & + \frac{1}{2}\rho A \int_0^L \left(\int_0^x \frac{\partial \theta(x,t)}{\partial t} \cos\left[\theta(x,t)\right] \mathrm{d}x + w_0 \omega \cos\left(\omega t\right) \right)^2 \mathrm{d}x, \end{aligned} \tag{7}$$

in which ρ denotes the mass density and A stands for the cross-sectional area.

The motion constraints are modelled via linear springs with very large stiffness coefficients. Hence, the work of the motion constraints (both sides) can be mathematically represented as

$$\delta W_c = -\int_0^L \left\{ k_1 \cos\theta \int_x^L \left[\delta_D(x - x_c) \mathrm{H}\left(\left| \int_0^x \sin\theta \, \mathrm{d}x \right| - g_0 \right) \mathrm{sgn}\left(\int_0^x \sin\theta \, \mathrm{d}x \right) \left(\left| \int_0^x \sin\theta \, \mathrm{d}x \right| - g_0 \right) \right] \mathrm{d}x \right\} \delta\theta \, \mathrm{d}x \tag{8}$$

where H denotes the Heaviside function, sgn stands for the Sign function, δ_D represents the Dirac Delta function, and the vertical bars, i.e. ||, indicate the absolute value.

Employing generalised Hamilton's principle

$$\int_{t_1}^{t_2}\left(\delta KE-\delta \Pi+\delta W_v+\delta W_c\right)\mathrm{d}t=0, \tag{9}$$

one can derive the equation governing the rotational motion of the cantilever under transverse base-excitation and subject to motion constraints as

$$\begin{aligned}&\rho I\frac{\partial^2\theta}{\partial t^2}-EI\frac{\partial^2\theta}{\partial x^2}-\eta I\frac{\partial^3\theta}{\partial t\partial x^2}-\rho A\sin\theta\int_L^x\int_0^x\left[\left(\frac{\partial\theta}{\partial t}\right)^2\cos\theta+\frac{\partial^2\theta}{\partial t^2}\sin\theta\right]\mathrm{d}x\,\mathrm{d}x\\&\quad+\rho A\cos\theta\int_L^x\left\{w_0\omega^2\sin(\omega t)+\int_0^x\left[\left(\frac{\partial\theta}{\partial t}\right)^2\sin\theta-\frac{\partial^2\theta}{\partial t^2}\cos\theta\right]\mathrm{d}x\right\}\mathrm{d}x\\&\quad+k_1\cos\theta\int_x^L\left[\delta_D(x-x_c)\mathrm{H}\left(\left|\int_0^x\sin\theta\,\mathrm{d}x\right|-g_0\right)\mathrm{sgn}\left(\int_0^x\sin\theta\,\mathrm{d}x\right)\left(\left|\int_0^x\sin\theta\,\mathrm{d}x\right|-g_0\right)\right]\mathrm{d}x=0\end{aligned} \tag{10}$$

Introducing the following dimensionless quantities

$$\alpha=\frac{AL^2}{I},\ x^*=\frac{x}{L},\ x_c^*=\frac{x_c}{L},\ t^*=\frac{t}{\tau},\ \eta_d=\frac{\eta}{E\tau},\ w_0^*=\frac{w_0}{L},\ \omega_e=\omega\tau,\ g_0^*=\frac{g_0}{L},\ K_1=\frac{k_1L^3}{EI}, \tag{11}$$

where $\tau=\sqrt{\rho AL^4/(EI)}$, inserting them in Eq. (10) and disregarding the asterisk notation results in

$$\begin{aligned}&\frac{1}{\alpha}\frac{\partial^2\theta}{\partial t^2}-\frac{\partial^2\theta}{\partial x^2}-\eta_d\frac{\partial^3\theta}{\partial t\partial x^2}-\sin\theta\int_1^x\int_0^x\left[\left(\frac{\partial\theta}{\partial t}\right)^2\cos\theta+\frac{\partial^2\theta}{\partial t^2}\sin\theta\right]\mathrm{d}x\,\mathrm{d}x\\&\quad+\cos\theta\int_1^x\left\{w_0\omega_e\sin(\omega_e t)+\int_0^x\left[\left(\frac{\partial\theta}{\partial t}\right)^2\sin\theta-\frac{\partial^2\theta}{\partial t^2}\cos\theta\right]\mathrm{d}x\right\}\mathrm{d}x\\&\quad+K_1\cos\theta\int_x^1\left[\delta_D(x-x_c)\mathrm{H}\left(\left|\int_0^x\sin\theta\,\mathrm{d}x\right|-g_0\right)\mathrm{sgn}\left(\int_0^x\sin\theta\,\mathrm{d}x\right)\left(\left|\int_0^x\sin\theta\,\mathrm{d}x\right|-g_0\right)\right]\mathrm{d}x=0\end{aligned} \tag{12}$$

Wiring the equation of motion in dimensionless form allows for a general parametric analysis [21]. In order to be able to examine the nonlinear dynamical characteristics of the cantilever numerically, Eq. (12) is reduced to a discretised set nonlinear ordinary differential

equations (ODEs) utilising the Galerkin technique. To this end, the cantilever centreline rotation is expanded as

$$\begin{aligned}&\theta(x,t)=\sum_{m=1}^{N}p_m(t)\psi_m(x),\\&\psi_m(x)=\left[\sinh\left(\beta_m x\right)+\sin\left(\beta_m x\right)-\chi_m\left(\cosh\left(\beta_m x\right)-\cos\left(\beta_m x\right)\right)\right],\end{aligned}\tag{13}$$

where $p_m(t)$ denotes the mth generalised coordinate for the rotational motion and $\chi_m=\left[\cosh\left(\beta_m\right)+\cos\left(\beta_m\right)\right]/\left[\sinh\left(\beta_m\right)+\sin\left(\beta_m\right)\right]$; β_m is the mth root of the equation $1+\cosh\left(x\right)\cos\left(x\right)=0$.

Substitution of Eq. (13) into the equation of motion, i.e. Eq. (12), and application of the Galerkin method results in

$$\begin{aligned}&\frac{1}{\alpha}\sum_{n=1}^{N}\left(\int_0^1\psi_m\psi_n\,\mathrm{d}x\right)\ddot{p}_n-\sum_{n=1}^{N}\left(\int_0^1\psi_m\psi_n''\,\mathrm{d}x\right)p_n-\eta_d\sum_{n=1}^{N}\left(\int_0^1\psi_m\psi_n''\,\mathrm{d}x\right)\dot{p}_n\\&-\int_0^1\psi_m\left\{\sin\left(\sum_{n=1}^{N}p_n(t)\psi_n(x)\right)\int_1^x\int_0^x\left[\left(\frac{\partial}{\partial t}\left(\sum_{n=1}^{N}p_n(t)\psi_n(x)\right)\right)^2\cos\left(\sum_{n=1}^{N}p_n(t)\psi_n(x)\right)\right.\right.\\&\qquad\left.\left.+\frac{\partial^2}{\partial t^2}\left(\sum_{n=1}^{N}p_n(t)\psi_n(x)\right)\sin\left(\sum_{n=1}^{N}p_n(t)\psi_n(x)\right)\right]\mathrm{d}x\,\mathrm{d}x\right\}\mathrm{d}x\\&+\int_0^1\psi_m\left\{\cos\left(\sum_{n=1}^{N}p_n(t)\psi_n(x)\right)\int_1^x\left(w_0\omega_e\sin\left(\omega_e t\right)+\int_0^x\left[\left(\frac{\partial}{\partial t}\left(\sum_{n=1}^{N}p_n(t)\psi_n(x)\right)\right)^2\sin\left(\sum_{n=1}^{N}p_n(t)\psi_n(x)\right)\right.\right.\\&\qquad\left.\left.-\frac{\partial^2}{\partial t^2}\left(\sum_{n=1}^{N}p_n(t)\psi_n(x)\right)\cos\left(\sum_{n=1}^{N}p_n(t)\psi_n(x)\right)\right]\right)\mathrm{d}x\,\mathrm{d}x\right\}\mathrm{d}x\\&+\int_0^1\psi_m\left\{K_1\cos\left(\sum_{n=1}^{N}p_n(t)\psi_n(x)\right)\int_x^1\left[\delta_D(x-x_c)\mathrm{H}\left(\left|\int_0^x\sin\left(\sum_{n=1}^{N}p_n(t)\psi_n(x)\right)\mathrm{d}x\right|-g_0\right)\right.\right.\\&\qquad\left.\left.\times\mathrm{sgn}\left(\int_0^x\sin\left(\sum_{n=1}^{N}p_n(t)\psi_n(x)\right)\mathrm{d}x\right)\left(\left|\int_0^x\sin\left(\sum_{n=1}^{N}p_n(t)\psi_n(x)\right)\mathrm{d}x\right|-g_0\right)\right]\mathrm{d}x\right\}\mathrm{d}x=0,\end{aligned}\tag{14}$$

$m=1, 2, \ldots, N$.

In order to ensure accurate results even at very large-amplitude oscillations, the trigonometric functions of θ are kept intact as they are integrated from 0 to 1, which results in substantially large equations of motion. The presence of such large equations and nonlinear inertial terms makes the numerical simulation even more challenging. In this study, 5 generalised coordinates are retained in the rotational motion series expansion, resulting in a 5-degree-of-freedom (DOF) system which ensures converged results; in other words, the contribution of higher modes (more than 5) to the cantilever response is small enough that can be safely neglected. After obtaining the amplitude of the rotational motion, the longitudinal and transverse displacements are calculated using Eq. (1). The 5-DOF discretised system of equations is solved numerically via use of a pseudo-arclength continuation technique; additionally, a stability analysis was conducted using Floquet theory. The employed method used is capable of capturing all types of periodic motions as well as detecting different bifurcations [22].

3. Numerical results

The nonlinear large-amplitude oscillations of the cantilever with and without motion constraints are studied in this section. In order to better illustrate the capability of the developed model in capturing very large-amplitude oscillations of the cantilever, the motion constraint is initially removed and the nonlinear resonant response of the system under base-excitation is examined; this is discussed in sub-section 3.1. Then, the detailed nonlinear response of the cantilever subject to motion constraint is examined and discussed in sub-section 3.2. The numerical results are obtained for a cantilever of dimensions h=1 mm, b=5h,

and L=200h. It should be mentioned here once again that all the reported values in this section are dimensionless as defined in Eq. (11) with the asterisk notation being dropped for convenience.

3.1. Nonlinear response of the cantilever without motion constraint

In the absence of a motion constraint, the cantilever is free to undergo large-amplitude oscillations. The transverse amplitude of oscillation depends of course on the base-excitation amplitude. Figure 2 shows the nonlinear frequency-amplitude plots of the cantilever undergoing large-amplitude oscillations due to transverse base-excitation. For this case, w_0=0.018 and η_d=0.0057. Sub-figures (a, b) show the cantilever tip transverse and longitudinal displacements while sub-figure (c) shows the cantilever tip angle. It is worth mentioning that solving the model developed in Section 2 results in the value of centreline angle. Having obtained the centreline angle, the transverse and longitudinal displacements are calculated via using Eq. (1). As seen in Fig. 2, the system shows a weak nonlinear hardening behaviour. Furthermore, sub-figure (c) shows that the tip angle maximum value is more than $\pi/2$, indicating that the tip of the cantilever bends more than 90° at large-amplitude oscillations. This is the main advantage of the model developed in this study, as it overcomes the limitation of the classical nonlinear transverse model of the cantilever (i.e. the tip angle being between -$\pi/2$ and $\pi/2$). To better illustrate the oscillation of the cantilever, the system motion is captured at different frames in one full period for points P_1, P_2, and P_3, and plotted in Fig. 3. As seen in sub-figure (a), the cantilever longitudinal displacement is much smaller than its transverse

displacement; however, at larger oscillation amplitudes, for instance sub-figure (c), the longitudinal displacement becomes comparable to the transverse displacement.

3.2. Nonlinear response of the cantilever with motion constraint

This section examines the nonlinear resonant response of the cantilever in the presence of a motion constraint at x_c=0.2. The frequency-amplitude diagrams are constructed for different cases and the effect of different parameters is examined in detail.

Figure 4 shows a comparison between constrained and unconstrained motion of the cantilever in the primary resonance region. For this case, an initial gap width of 0.03 is considered, i.e. g_0=0.03. Furthermore, a large spring stiffness coefficient is considered, i.e. K_1=2.0E4, to properly model the effect of the motion constraint. The base-excitation amplitude is set to w_0=0.018 while its frequency (ω_e) is varied in the vicinity of the fundamental natural frequency of the cantilever, i.e. ω_1=3.5160. As seen in sub-figure (a), the presence of a motion constraint reduces the amplitude of the oscillation, but yields wider resonance frequency band. This is particularly interesting and useful for energy harvesting applications. More specifically, one of the techniques used in increasing the efficiency of vibration-based energy harvesters is to increase the band of resonance vibration, i.e. increase the interval at which the amplitude is larger than a certain value. If a transverse displacement threshold of 0.45 is considered, the cantilever system without constraint undergoes oscillations of amplitude larger than 0.45 in the frequency range of 0.980 < ω_e/ω_1 < 1.031; however, the constrained cantilever system undergoes oscillations of amplitude larger than 0.45 in the frequency range of 0.980 < ω_e/ω_1 <

1.160, i.e. 3.5 times the range of unconstrained system. Comparing the area under the curve for both constrained and unconstrained system in the frequency ratio range shown in the figure (i.e. 0.90 < ω_e/ω_1 < 1.18) reveals a value of for the 0.0790 unconstrained system and a value of 0.1292 for the constrained, i.e. an increase of 63.5 %.

The detailed dynamical characteristics of the constrained cantilever at two different excitation frequencies, ω_e/ω_1=0.9775 and 1.1030, are illustrated in Figs. 5 and 6, respectively. ω_e/ω_1=0.9775 is in the resonance region before hitting the motion constraint while ω_e/ω_1=1.1030 is in the region where the cantilever is hitting the motion constraint. The goal here is to compare the time traces and phase-plane portraits of the cantilever motion before and after hitting the motion constraint. As seen in Fig. 5, the cantilever displays smooth periodic response in the region where there is not contact between the cantilever and the constraint. However, as seen in Fig. 6, the dynamical characteristics of the cantilever in the region where it hits the constraint are totally different, showing non-smooth vibrational behaviour.

It would be interesting to compare the response of the cantilever subject to motion constraint at both sides to that subject to motion constraint only at one side; the comparison between the two cases is shown in Fig. 7. As seen, when the cantilever motion is constrained from both sides, the change in the slope of the resonance response after hitting the constraint is larger compared to the case with one-side constraint. Furthermore, the cantilever with constraints at both sides shows wider resonance frequency band compared to the cantilever with a constraint only at one side. It should be noted that for the rest of the figures in this

paper, it is assumed that the cantilever is constrained at both sides. It is important to note that asymmetric motions can arise even in oscillators with perfectly symmetric properties.

As mentioned in the previous section, in this study the motion constraints are modelled as linear springs located at distance x_c from the clamped base and at both sides of the cantilever with a gap (clearance) g_0. To this end, the spring stiffness coefficient should be large enough to ensure that the spring is a realistic representative of the motion constraint. The effect of the spring stiffness coefficient on the frequency-amplitude diagrams of the constrained cantilever is shown in Fig. 8; the frequency-amplitude plot of the unconstrained cantilever is plotted as well for better comparison. As seen, due to increased stiffness coefficient, the change in slope of the frequency-response becomes sharper when the cantilever hits the motion constraint. Additionally, the frequency band of resonance increases with increasing stiffness coefficient. It is interesting to note that the resonance response of the constrained cantilever changes dramatically when K_1 is increased from 2.0E2 to 2.0E3; however, a smaller change in the resonance response is observed as K_1 is increased from 2.0E3 to 2.0E4. Increasing the stiffness coefficient even further, to 6.0E4, causes only very slight change in the resonance response, indicating convergence. Hence, K_1 = 2.0E4 can be selected as the stiffness of the constraint since it gives a reasonable approximation of the motion constraint while allowing for smooth numerical simulations.

The effect of the gap width (clearance) of the motion constraint on the nonlinear resonance response of the constrained cantilever is depicted in Fig. 9. As seen, as the gap width is decreased, the cantilever hits the motion constraint at smaller oscillation amplitudes; as a

result, the change in slope of the resonance response occurs at smaller excitation frequencies. Furthermore, as the gap width is decreased, the resonance frequency band increases and the peak amplitude occurs at larger excitation frequencies.

Figure 10 shows the effect of the base-excitation amplitude on the nonlinear frequency-amplitude response of the constrained cantilever. It is seen that at a small base-excitation amplitude of 0.005, the cantilever does not hit the motion constraint, hence displaying a smooth response. At larger base-excitation amplitudes, on the other hand, the cantilever does hit the motion constraint causing a sharp change in the slope of the resonance response. As seen, by increasing the base-excitation amplitude, the resonance frequency band increases and the peak amplitude occurs at larger excitation frequencies.

The frequency-amplitude plots of the constrained cantilever for two locations of the motion constraint are illustrated in Fig. 11. As seen, as the motion constraint is moved slightly to the right (i.e. further away from the base), the cantilever hits it at smaller excitation frequencies. Furthermore, the peak amplitude occurs at larger excitation frequencies as the constraint is moved to the right on the *x* axis.

The effect of the material damping coefficient η_d on the resonance response of the constrained cantilever is shown in Fig. 12. As seen, as η_d is increased, the multi-valued resonance region becomes wider and the peak amplitude occurs at smaller excitation frequencies. It is interesting to note that increasing η_d from 0.006 to 0.007 causes a further reduction in the amplitude compared to the case when η_d is increased from 0.005 to 0.006.

4. Conclusions

The nonlinear large-amplitude oscillation of a cantilever under base excitation has been examined in the presence of motion-limiting constraints on both sides of the cantilever. Hamilton's principle is employed to derive the equation governing the rotational motion of the cantilever centreline, based on the Euler-Bernoulli beam theory and centreline inextensibility assumption. The equation of motion is discretised through use of the Galerkin technique; the trigonometric functions in the equation of motion are kept intact to ensure accurate results. The discretised equations are solved making use of a continuation technique, while examining the effect of various system parameters.

It is shown that unlike other nonlinear models of the cantilever (based on transverse motion), the present model can predict large-amplitude oscillations even when the tip angle becomes larger than $\pi/2$. It is shown that the presence of a motion constraint reduces the amplitude of the oscillation and widens the band of resonance frequency vibration. Examining the effect of the stiffness of the motion constraint revealed that, as the stiffness is increased, the change in slope of the frequency-response becomes sharper when the cantilever hits the motion constraint; this results in widened resonance frequency band. Furthermore, it is shown that as the clearance between the motion constraint and the cantilever is increased, the change in slope of the frequency-response, due to hitting the motion constraint, occurs at smaller excitation frequencies. Examining the effect of the base-excitation amplitude on the nonlinear resonance response of the system shows that at small base-excitation amplitudes the cantilever does not hit the motion constraint; as the base-excitation amplitude is increased to larger

amplitudes, the cantilever hits the motion constraint causing a change in the slope of the frequency-amplitude. Additionally, due to increased base-excitation amplitude, the resonance frequency band increases and the peak amplitude occurs at larger excitation frequencies. If the motion constraint is moved further away from the clamped end, the cantilever hits it at smaller excitation frequencies and the resonance peak occurs at larger excitation frequencies.

Appendix A. Verification and Convergence

In order to verify the model and numerical results of the present study, a nonlinear static analysis is conducted on a cantilever without a stopper and the obtained results are compared to three-dimensional (3D) finite element analysis (FEA) results obtained using Abaqus/CAE. In order to examine very large-amplitude displacements, the cantilever is assumed to be under a concentrate tip load, always perpendicular to the beam. For such a system, the nonlinear dimensionless static equation of motion can be derived as

$$\frac{\partial^2\theta}{\partial x^2}+f_s\left[\cos\theta\int_x^1\left(\delta_D(x-1)\cos\theta\right)\mathrm{d}x+\sin\theta\int_x^1\left(\delta_D(x-1)\sin\theta\right)\mathrm{d}x\right]=0, \tag{15}$$

in which $f_s=fL^2/(EI)$ with f being the forcing amplitude (dimensional).

Using the same discretisation procedure and numerical technique introduced in Section 2, the nonlinear static response of the cantilever is obtained numerically. The cantilever nonlinear static deflection is also obtained using Abaqus/CAE, using continuum shell elements. The results obtained by the present study are compared to those obtained through 3D FEA and plotted in Figs. 13 and 14. The transverse and longitudinal displacements of the cantilever tip are shown in Fig. 13 for the two models. As seen, the model developed in this study predicts almost the same displacements as the nonlinear 3D FEA. Additionally, the deformed configuration of the cantilever under various tip load magnitudes is plotted in Fig. 14 for the two models, again showing very similar predictions by the two models; it should be noted that x and z are dimensionless with respect to the length of the cantilever. Hence, the comparisons in Figs. 13 and 14 verify the developed model and numerical technique in the present study.

Furthermore, Fig. 15 shows the maximum strain in the cantilever as a function of x when f_s=7.68. In particular, the strain is calculated at z=-h/2, where it is maximum for the system under consideration, and plotted as a function of x. Referring to Fig. 14, it is seen that for f_s=7.68, the system undergoes very large-amplitude deformation. However, as seen in Fig. 15, even for such large deformation, the strains remain small.

A convergence analysis is shown in Fig. 16 showing a comparison between the frequency-amplitude diagrams of the system obtained using 5-degree-of-freedom (5-DOF) and 6-DOF discretised models of the system. As seen, both models predict almost the same response showing that taking into account 5 modes ensures converged results.

References

[1] Liu, H., Lee, C., Kobayashi, T., Tay, C. J., and Quan, C., 2012, "Piezoelectric MEMS-based wideband energy harvesting systems using a frequency-up-conversion cantilever stopper," Sensors and Actuators A: Physical, 186, pp. 242-248.

[2] Huicong, L., Chengkuo, L., Takeshi, K., Cho Jui, T., and Chenggen, Q., 2012, "Investigation of a MEMS piezoelectric energy harvester system with a frequency-widened-bandwidth mechanism introduced by mechanical stoppers," Smart Materials and Structures, 21(3), p. 035005.

[3] Moon, F. C., and Shaw, S. W., 1983, "Chaotic vibrations of a beam with non-linear boundary conditions," International Journal of Non-Linear Mechanics, 18(6), pp. 465-477.

[4] Shaw, S. W., and Holmes, P. J., 1983, "A periodically forced piecewise linear oscillator," Journal of Sound and Vibration, 90(1), pp. 129-155.

[5] Choi, Y. S., and Noah, S. T., 1988, "Forced periodic vibration of unsymmetric piecewise-linear systems," Journal of Sound and Vibration, 121(1), pp. 117-126.

[6] Heiman, M. S., Bajaj, A. K., and Sherman, P. J., 1988, "Periodic motions and bifurcations in dynamics of an inclined impact pair," Journal of Sound and Vibration, 124(1), pp. 55-78.

[7] Shaw, S. W., and Rand, R. H., 1989, "The transition to chaos in a simple mechanical system," International Journal of Non-Linear Mechanics, 24(1), pp. 41-56.

[8] Li, G. X., Rand, R. H., and Moon, F. C., 1990, "Bifurcations and chaos in a forced zero-stiffness impact oscillator," International Journal of Non-Linear Mechanics, 25(4), pp. 417-432.

[9] Natsiavas, S., 1990, "On the dynamics of oscillators with bi-linear damping and stiffness," International Journal of Non-Linear Mechanics, 25(5), pp. 535-554.

[10] Natsiavas, S., 1993, "Dynamics of Multiple-Degree-of-Freedom Oscillators With Colliding Components," Journal of Sound and Vibration, 165(3), pp. 439-453.

[11] Nigm, M. M., and Shabana, A. A., 1983, "Effect of an impact damper on a multi-degree of freedom system," Journal of Sound and Vibration, 89(4), pp. 541-557.

[12] Björkenstam, U., 1977, "Impact vibration of a bar," International Journal of Mechanical Sciences, 19(8), pp. 471-481.

[13] Masri, S., Mariamy, Y., and Anderson, J., 1981, "Dynamic response of a beam with a geometric nonlinearity," Journal of Applied Mechanics, 48(2), pp. 404-410.

[14] Metallidis, P., and Natsiavas, S., 2000, "Vibration of a continuous system with clearance and motion constraints," International Journal of Non-Linear Mechanics, 35(4), pp. 675-690.

[15] Liu, S., Cheng, Q., Zhao, D., and Feng, L., 2016, "Theoretical modeling and analysis of two-degree-of-freedom piezoelectric energy harvester with stopper," Sensors and Actuators A: Physical, 245, pp. 97-105.

[16] Soliman, M. S. M., Abdel-Rahman, E. M., El-Saadany, E. F., and Mansour, R. R., 2008, "A wideband vibration-based energy harvester," Journal of Micromechanics and Microengineering, 18(11), p. 115021.

[17] Halim, M. A., and Park, J. Y., 2014, "Theoretical modeling and analysis of mechanical impact driven and frequency up-converted piezoelectric energy harvester for low-frequency and wide-bandwidth operation," Sensors and Actuators A: Physical, 208, pp. 56-65.

[18] Wu, Y., Badel, A., Formosa, F., Liu, W., and Agbossou, A., 2014, "Nonlinear vibration energy harvesting device integrating mechanical stoppers used as synchronous mechanical switches," Journal of Intelligent Material Systems and Structures, 25(14), pp. 1658-1663.

[19] Nayfeh, A. H., and Pai, P. F., 2008, Linear and nonlinear structural mechanics, John Wiley & Sons.

[20] Farokhi, H., Ghayesh, M. H., and Hussain, S., 2016, "Large-amplitude dynamical behaviour of microcantilevers," International Journal of Engineering Science, 106, pp. 29-41.

[21] Abdalla, M. M., Reddy, C. K., Faris, W. F., and Gürdal, Z., 2005, "Optimal design of an electrostatically actuated microbeam for maximum pull-in voltage," Computers & structures, 83(15-16), pp. 1320-1329.
[22] Allgower, E. L., and Georg, K., 2003, Introduction to Numerical Continuation Methods, Society for Industrial and Applied Mathematics.

(a)

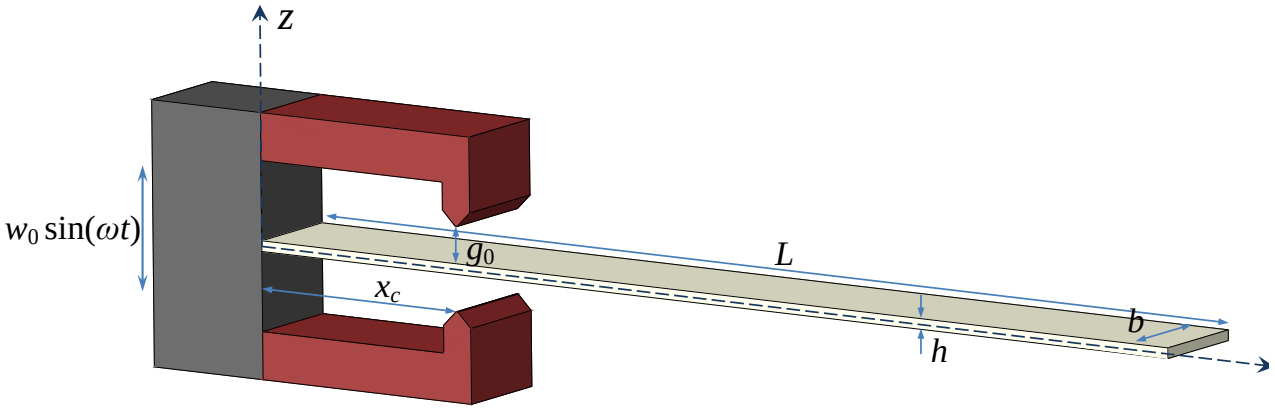

(b)

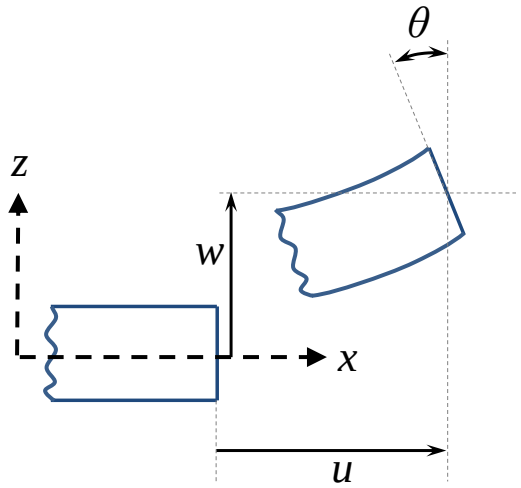

Fig.1. (a) Schematic of a cantilever under transverse base excitation subject to motion constraints; (b) deformed configuration of the system.

(a)

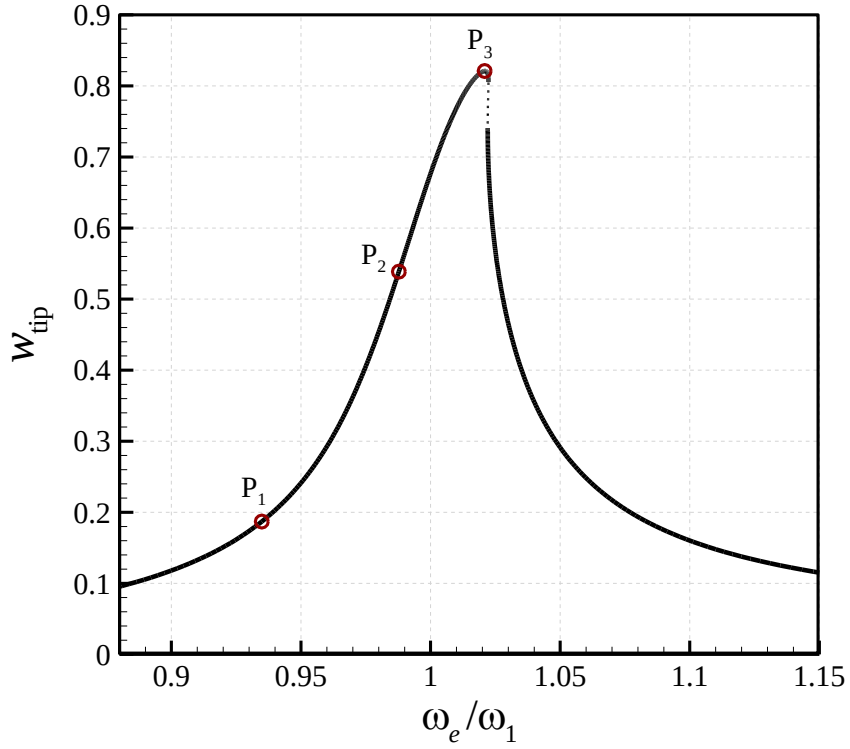
0.9
0.8
0.7
0.6
0.5
0.4
0.3
0.2
0.1
0
w_{tip}
P1
P2
P3
0.9
0.95
1
1.05
1.1
1.15
ω_e/ω_1

(b)

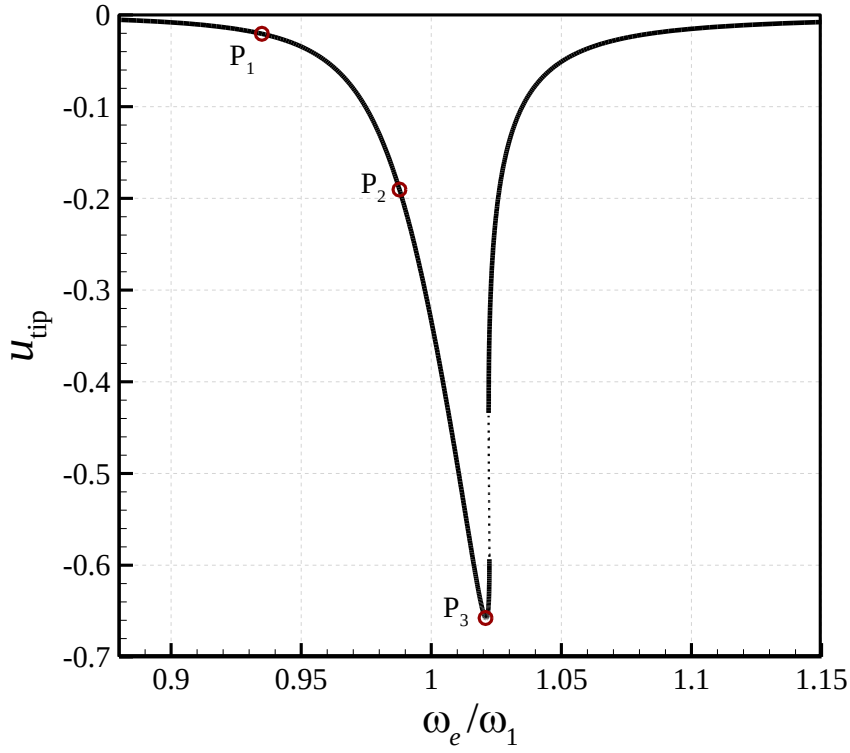
0
-0.1
-0.2
-0.3
-0.4
-0.5
-0.6
-0.7
u_{tip}
P1
P2
P3
0.9
0.95
1
1.05
1.1
1.15
ω_e/ω_1

(c)

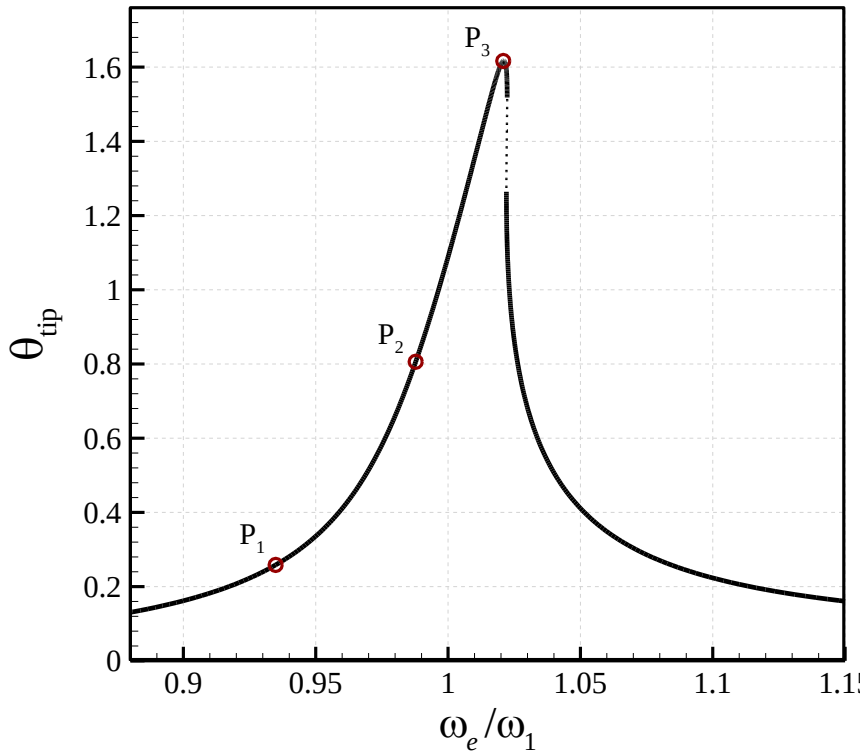

Fig.2. Frequency-amplitude plots of the cantilever without constraint; (a) maximum tip transverse displacement; (b) maximum tip longitudinal displacement; (c) maximum tip angle. Solid line showing stable solution while dotted line showing unstable one. P_1, P_1, and P_1, are points of interest which are examined in more detail in Fig. 3.

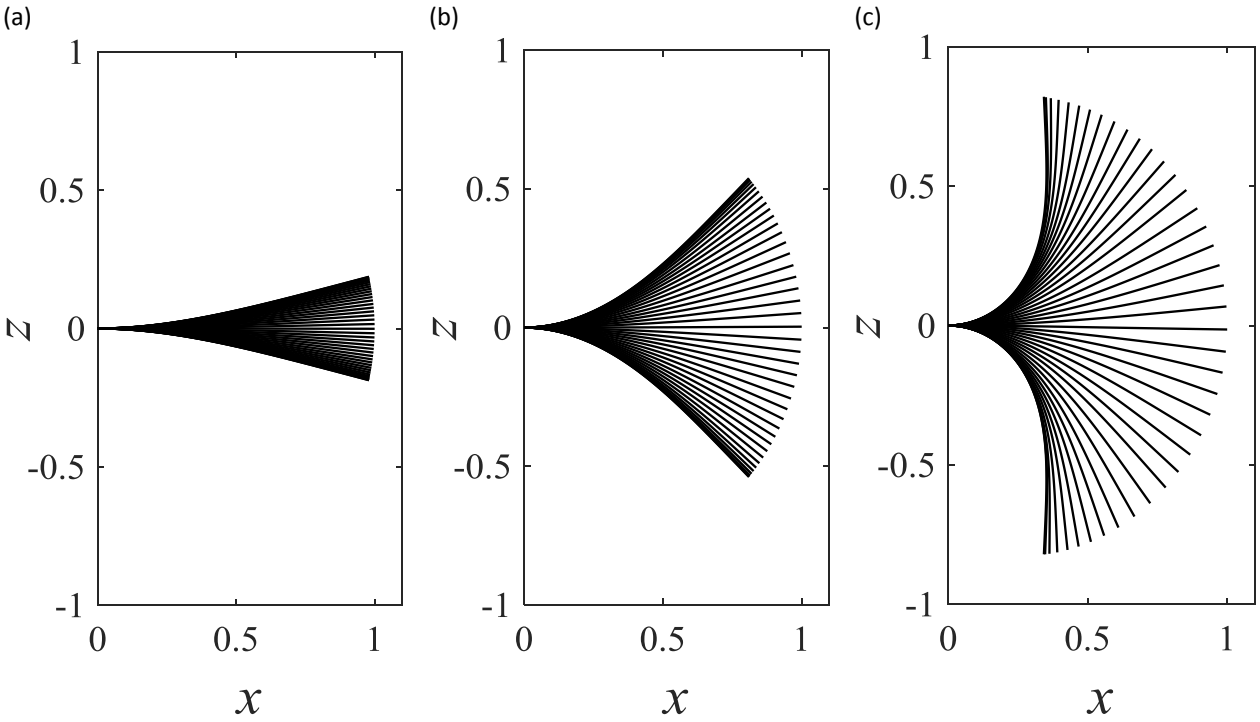

Fig.3. (a-c) Oscillation of the system of Fig. 2 at points P_1, P_2, and P_3, respectively.

(a)

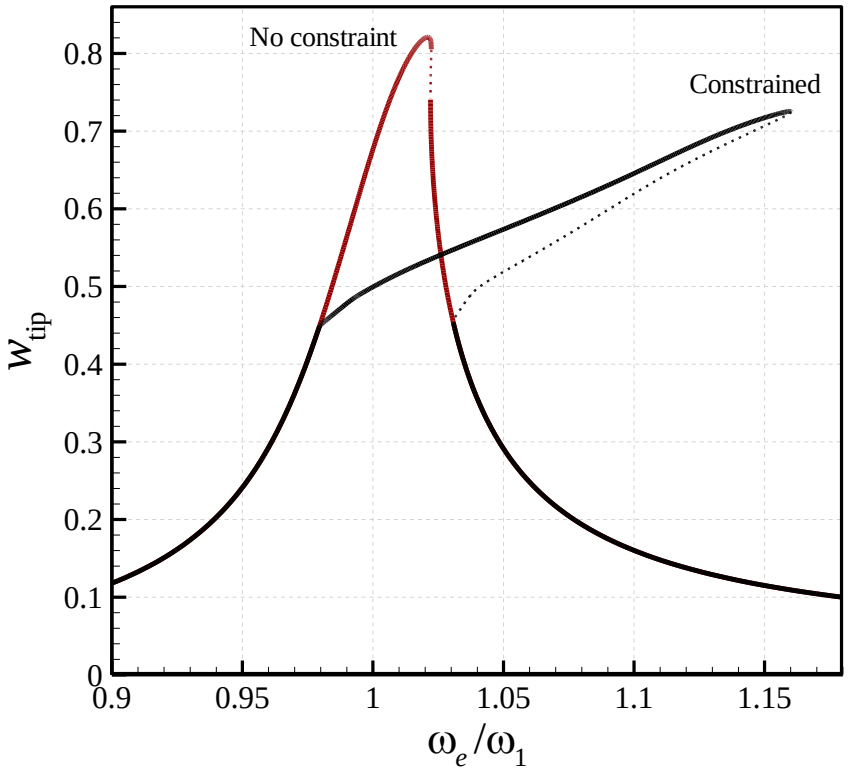
No constraint
Constrained
w_{tip}
ω_e/ω_1
0
0.1
0.2
0.3
0.4
0.5
0.6
0.7
0.8
0.9
0.95
1
1.05
1.1
1.15

(b)

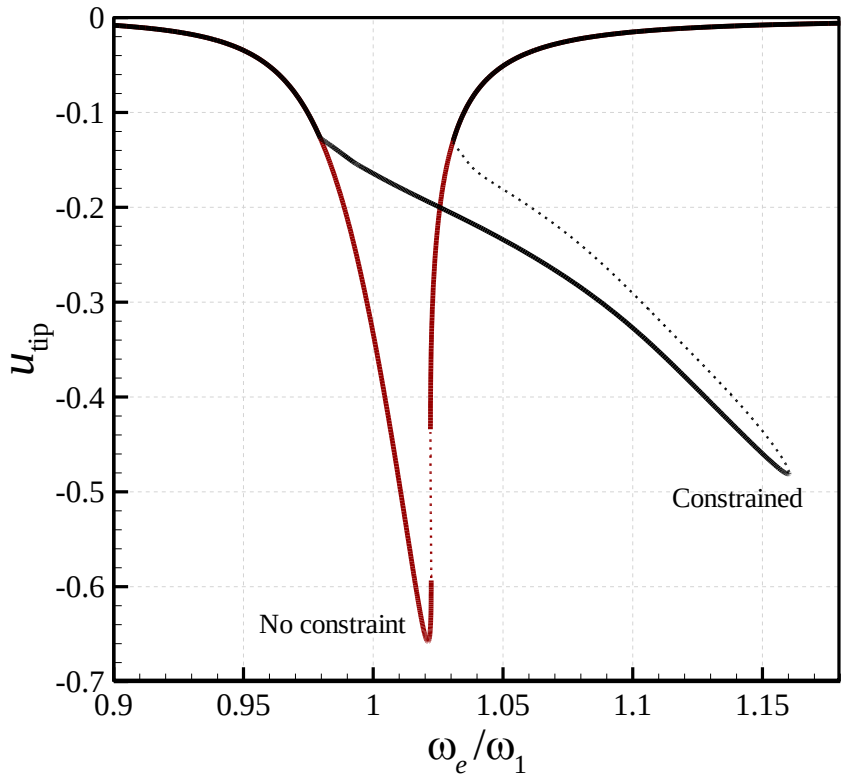
u_{tip}
ω_e/ω_1
Constrained
No constraint
0
-0.1
-0.2
-0.3
-0.4
-0.5
-0.6
-0.7
0.9
0.95
1
1.05
1.1
1.15

(c)

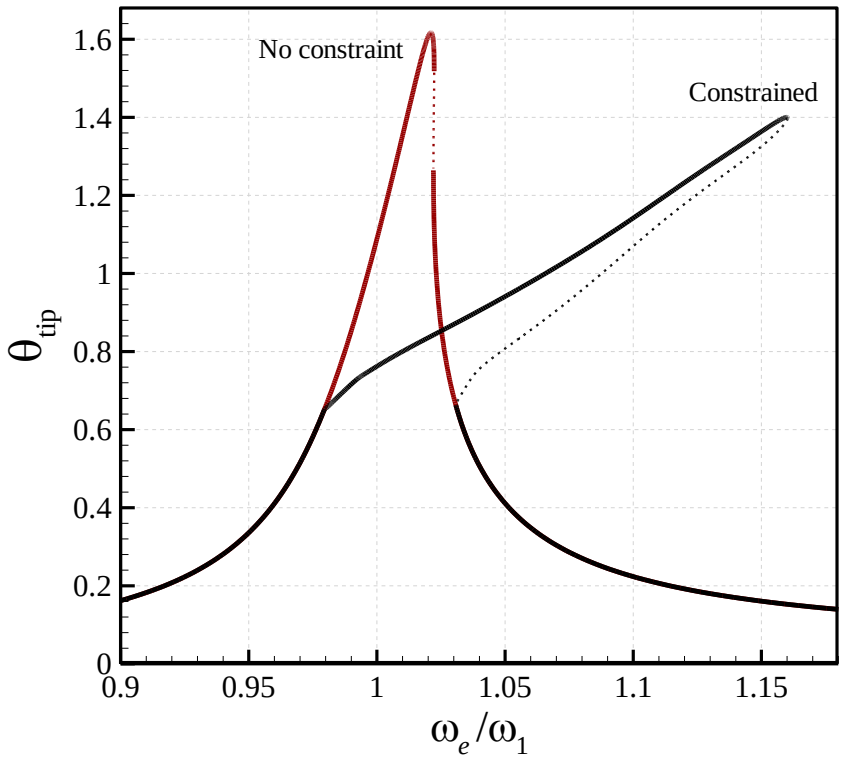

Fig.4. Comparison between the frequency-amplitude plots of the constrained cantilever to those of a cantilever with no constraint; (a) maximum tip transverse displacement; (b) maximum tip longitudinal displacement; (c) maximum tip angle. Solid line showing stable solution while dotted line showing unstable one. g_0=0.03, K_1=2.0E4, and w_0=0.018.

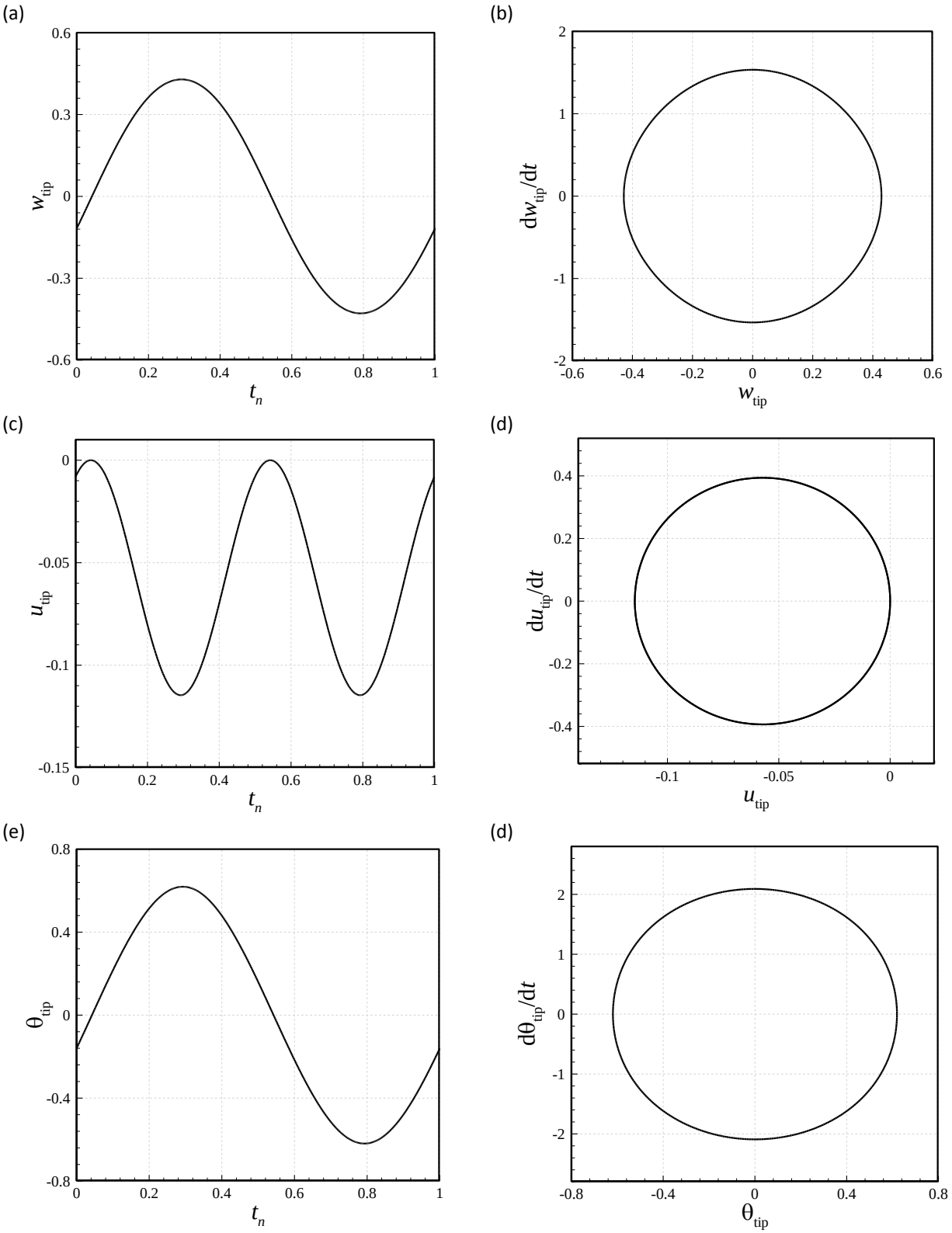

Fig.5. Details of the motion of the system of Fig. 4 at ω_e/ω_1=0.9775 (i.e. in the resonance region before hitting the motion constraint), showing respectively the time trace and phase-plane portrait of: (a, b) tip transverse displacement, (c, d) tip longitudinal displacement, and (e, f) tip angle. t_n denotes normalized time with respect to the period of the oscillation.

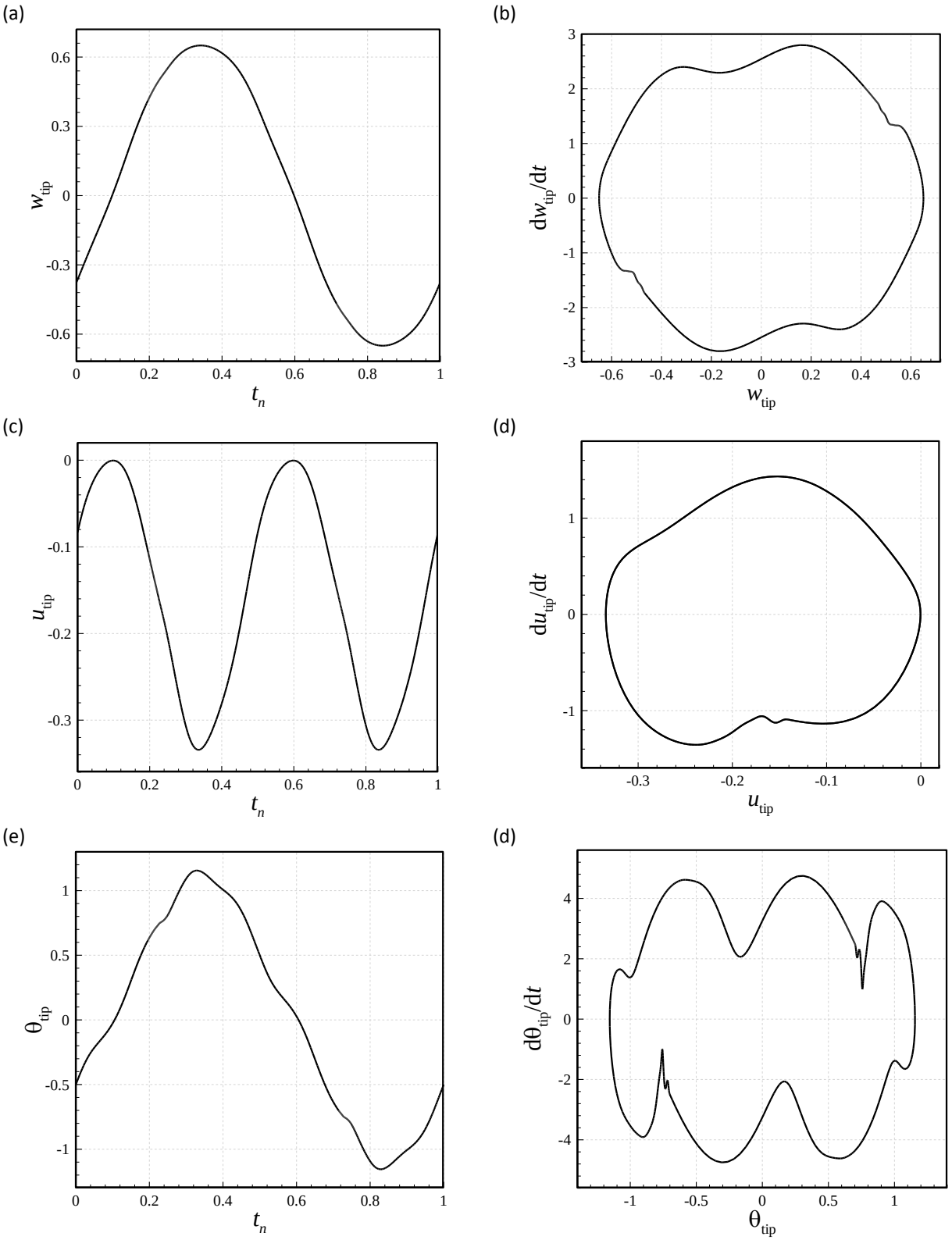

Fig.6. Details of the motion of the system of Fig. 4 at ω_e/ω_1=1.1030 (i.e. in the resonance region after hitting the motion constraint), showing respectively the time trace and phase-plane portrait of: (a, b) tip transverse displacement, (c, d) tip longitudinal displacement, and (e, f) tip angle. t_n denotes normalized time with respect to the period of the oscillation.

(a)

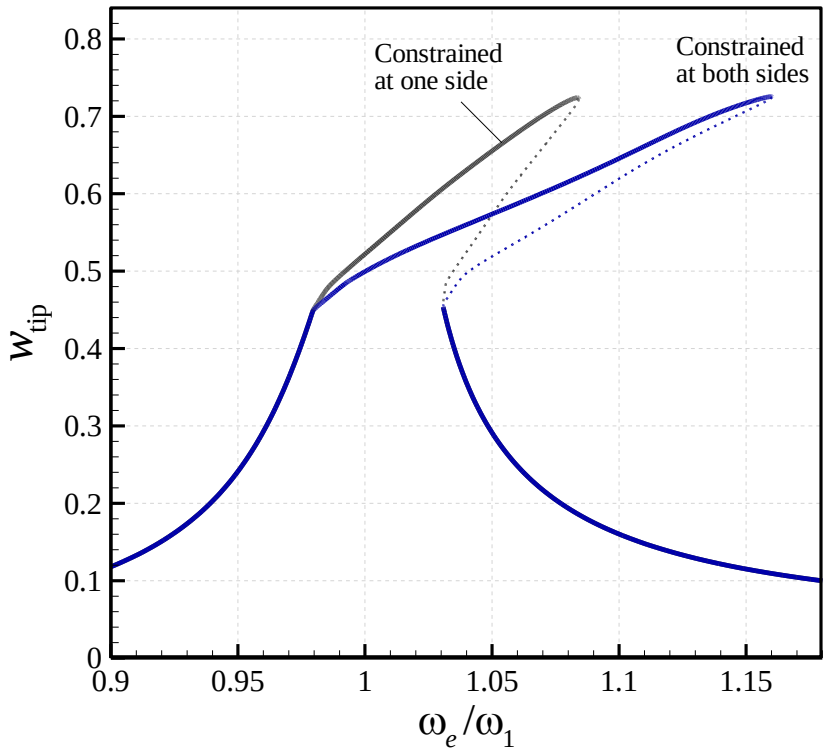

(b)

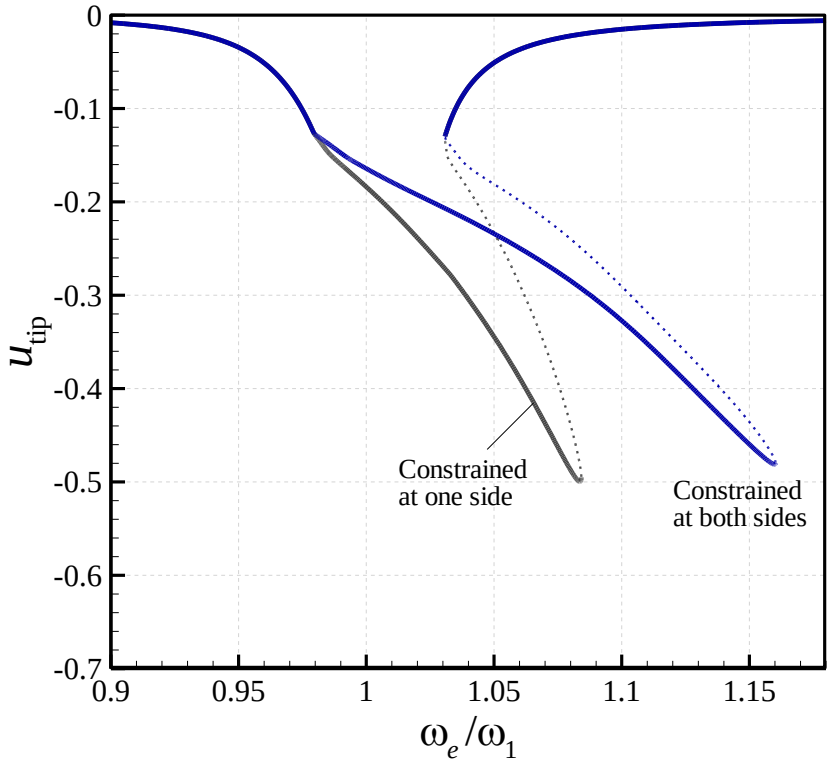

Fig.7. Comparison between the frequency-amplitude plots of the cantilever constrained at both sides to those of a cantilever constrained at one side; (a) maximum tip transverse displacement; (b) maximum tip longitudinal displacement. Solid line showing stable solution while dotted line showing unstable one. g_0=0.03, K_1=2.0E4, and w_0=0.018.

(a)

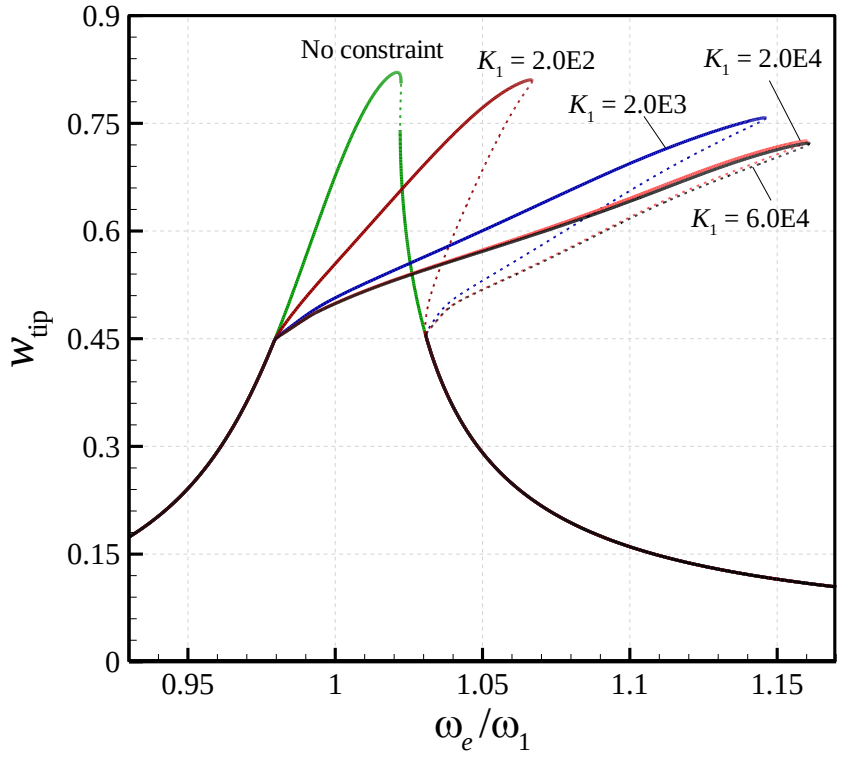

(b)

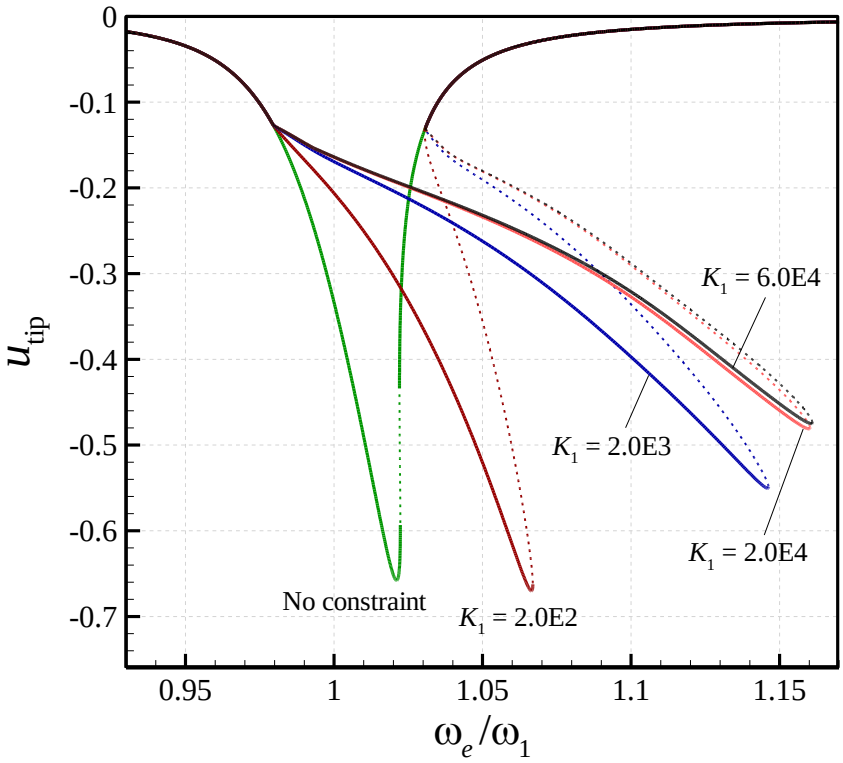

Fig.8. Effect of the motion constraint stiffness on frequency-amplitude plots of the constrained cantilever; (a) maximum tip transverse displacement; (b) maximum tip longitudinal displacement. Solid line showing stable solution while dotted line showing unstable one. g_0=0.03 and w_0=0.018.

(a)

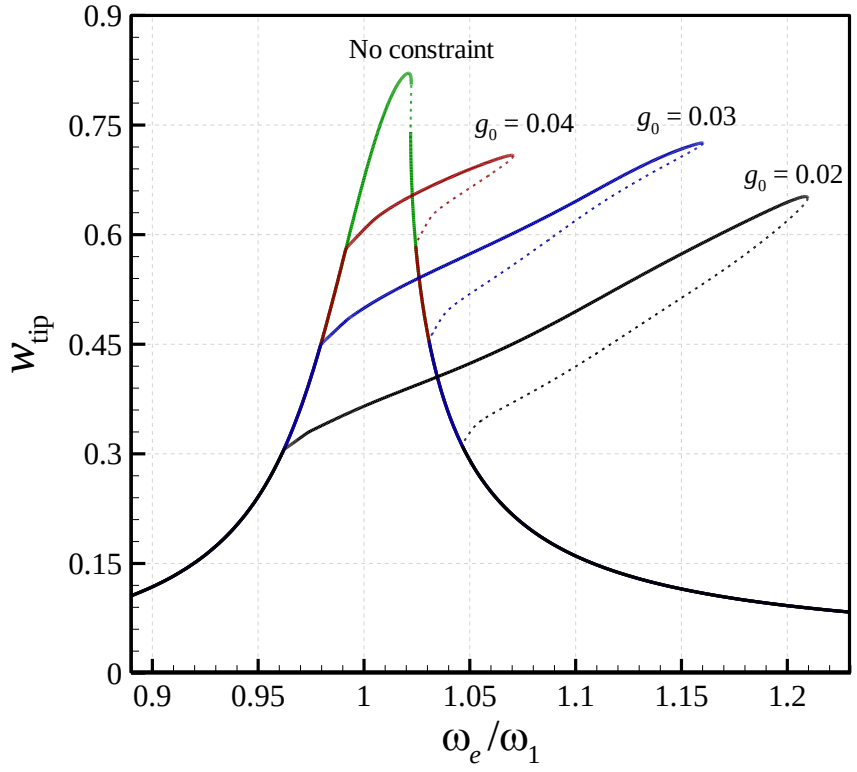

(b)

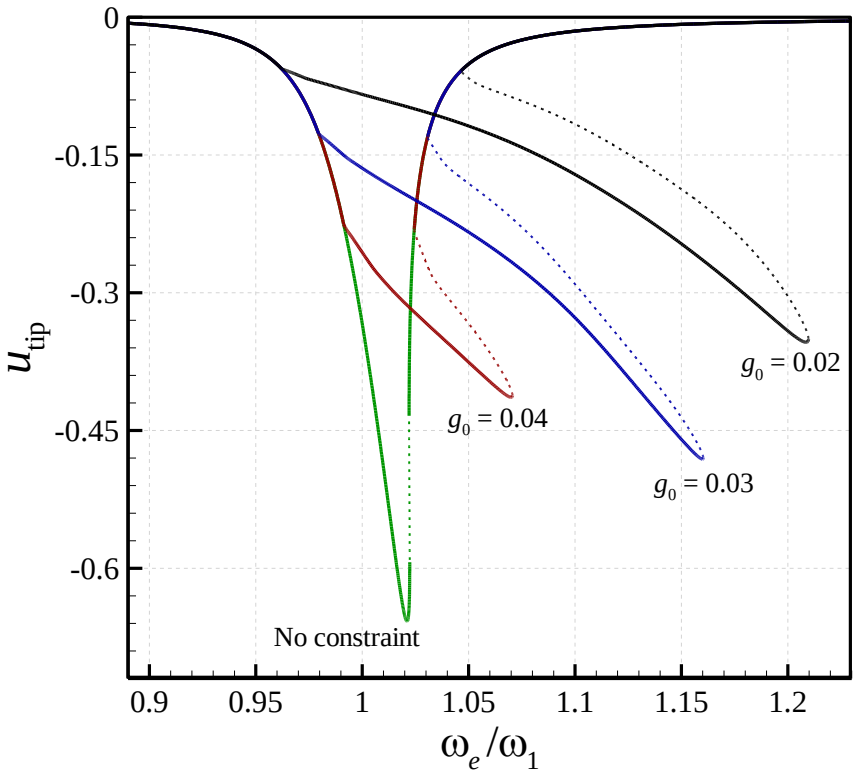

Fig.9. Effect of the motion constraint gap-width on the frequency-amplitude plots of the constrained cantilever; (a) maximum tip transverse displacement; (b) maximum tip longitudinal displacement. Solid line showing stable solution while dotted line showing unstable one. K_1=2.0E4 and w_0=0.018.

(a)

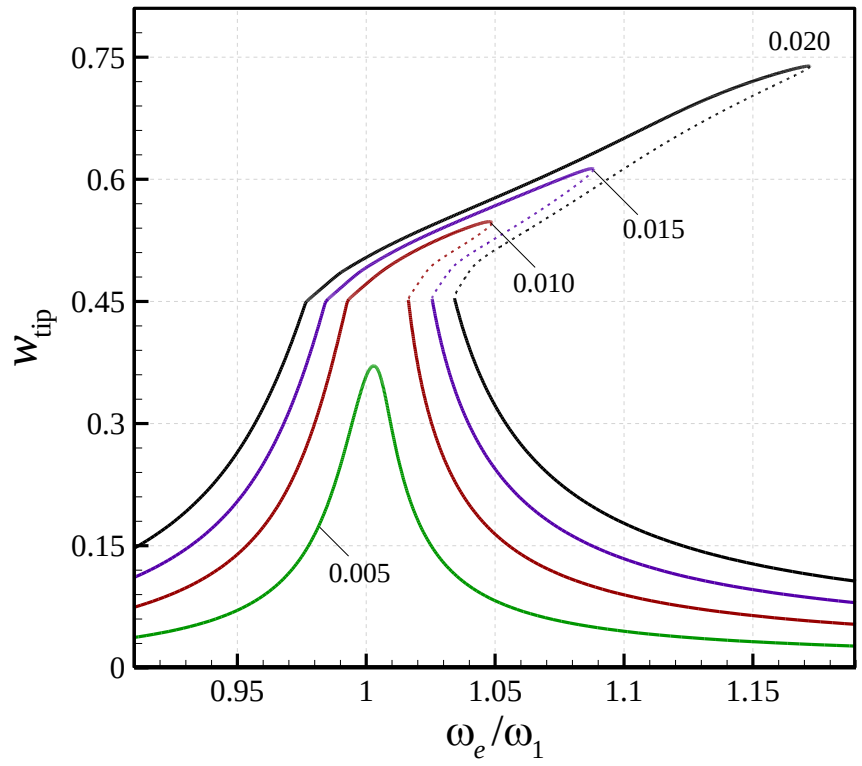

(b)

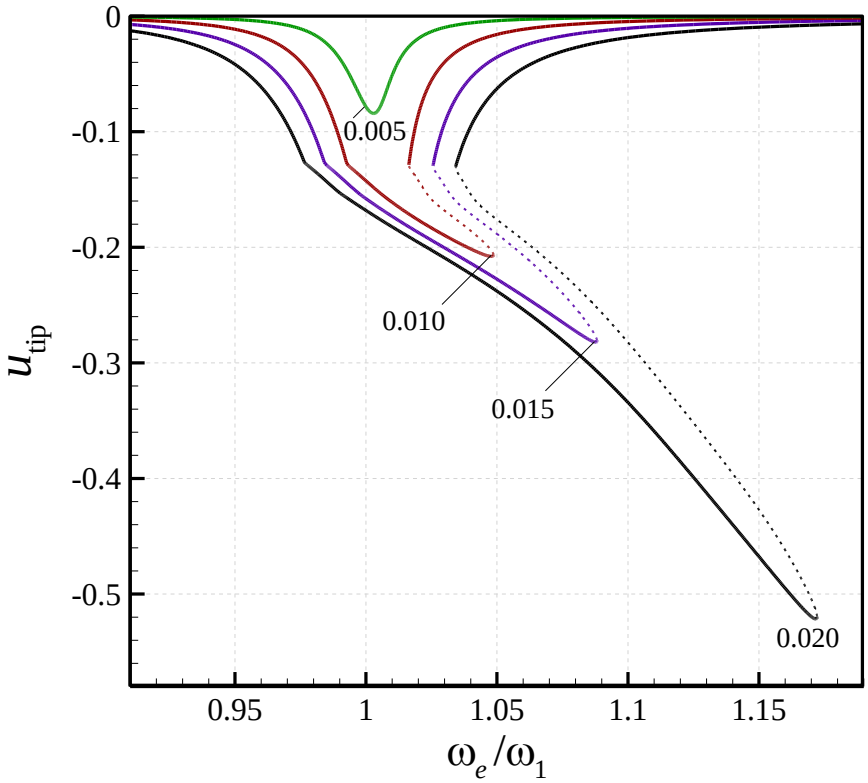

Fig.10. Effect of base-excitation amplitude on the frequency-amplitude plots of the constrained cantilever; (a) maximum tip transverse displacement; (b) maximum tip longitudinal displacement. Solid line showing stable solution while dotted line showing unstable one. g_0=0.03 and K_1=2.0E4.

(a)

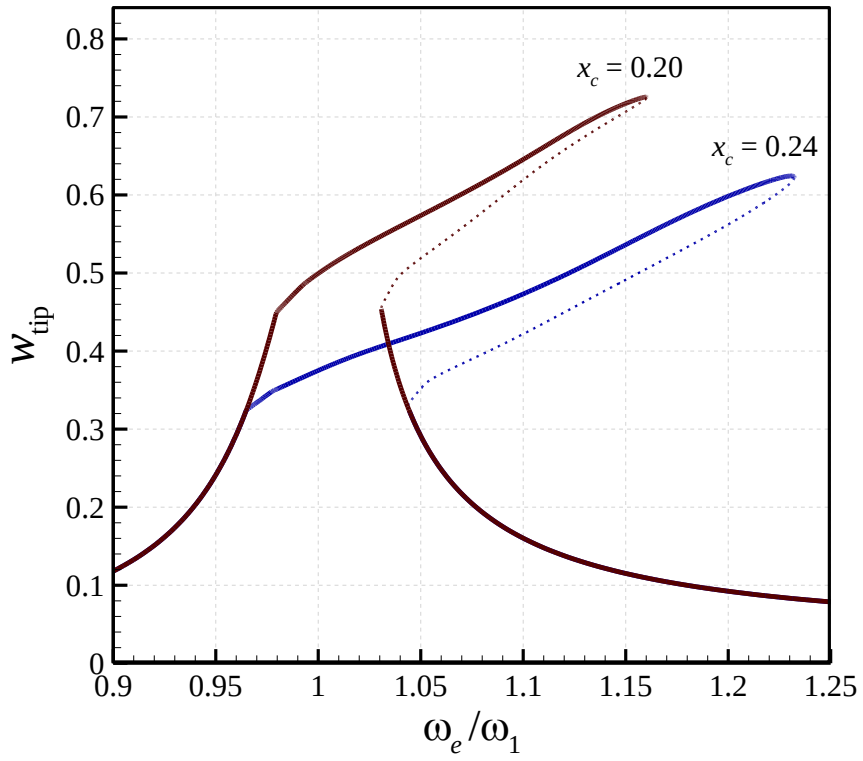

(b)

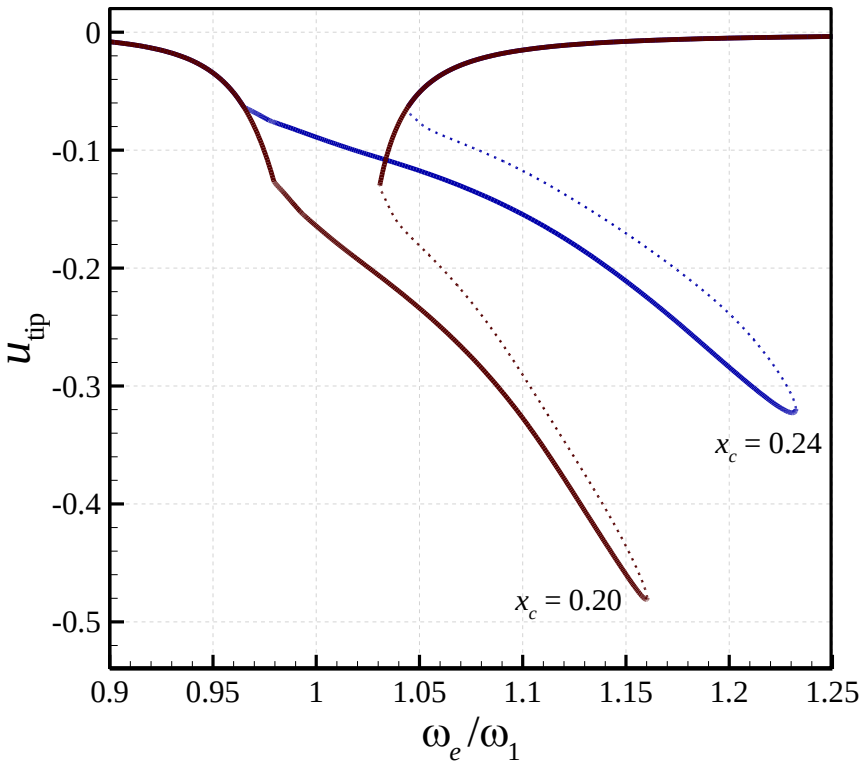

Fig.11. Effect of the position of the motion constraint on the frequency-amplitude plots of the cantilever; (a) maximum tip transverse displacement; (b) maximum tip longitudinal displacement. Solid line showing stable solution while dotted line showing unstable one. g_0=0.03, K_1=2.0E4, and w_0=0.018.

(a)

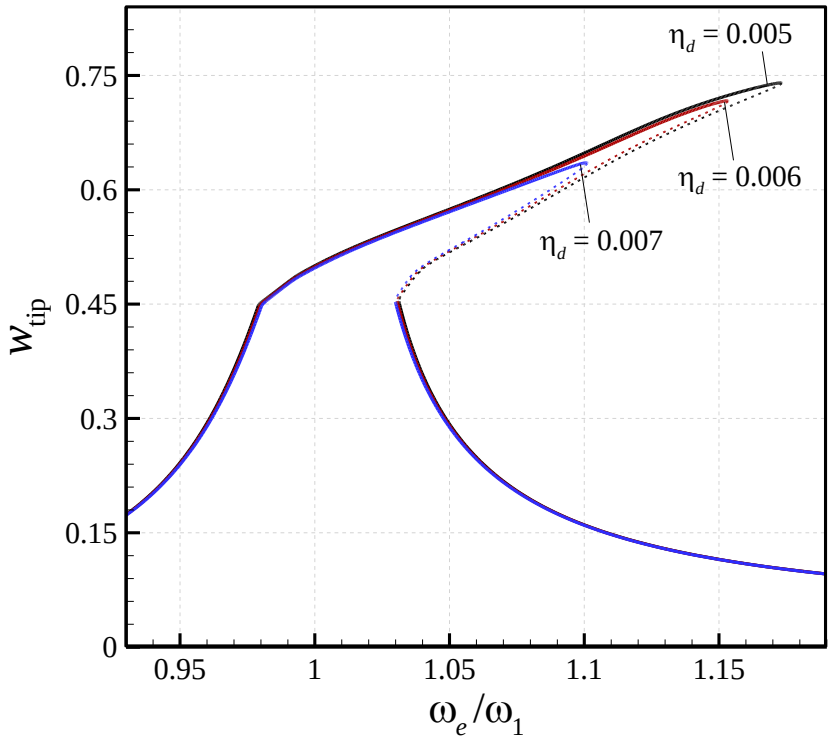

(b)

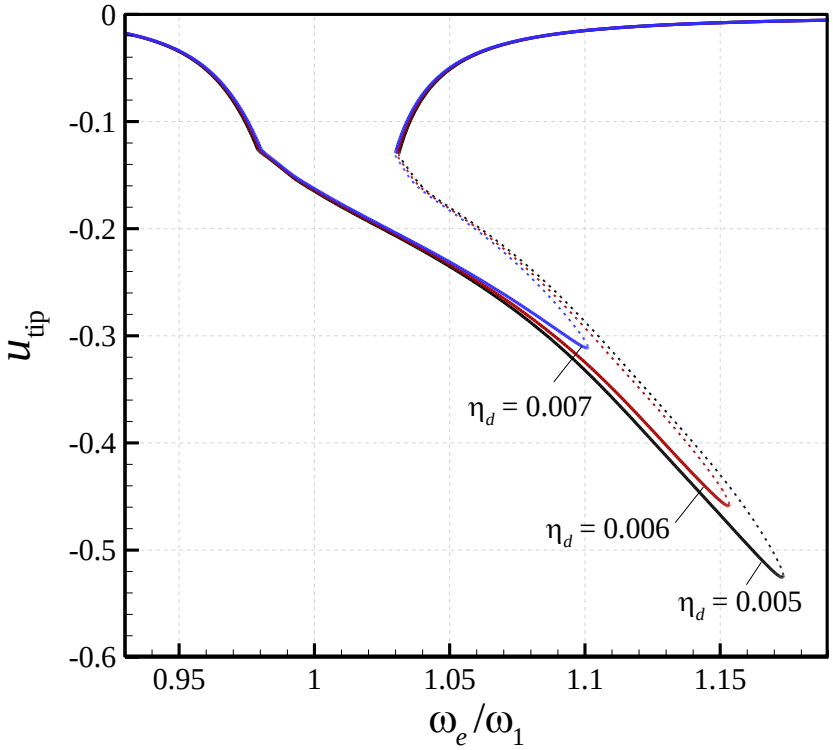

Fig.12. Effect of material damping coefficient on the frequency-amplitude plots of the constrained cantilever; (a) maximum tip transverse displacement; (b) maximum tip longitudinal displacement. Solid line showing stable solution while dotted line showing unstable one. g_0=0.03 and K_1=2.0E4, and w_0=0.018.

(a)

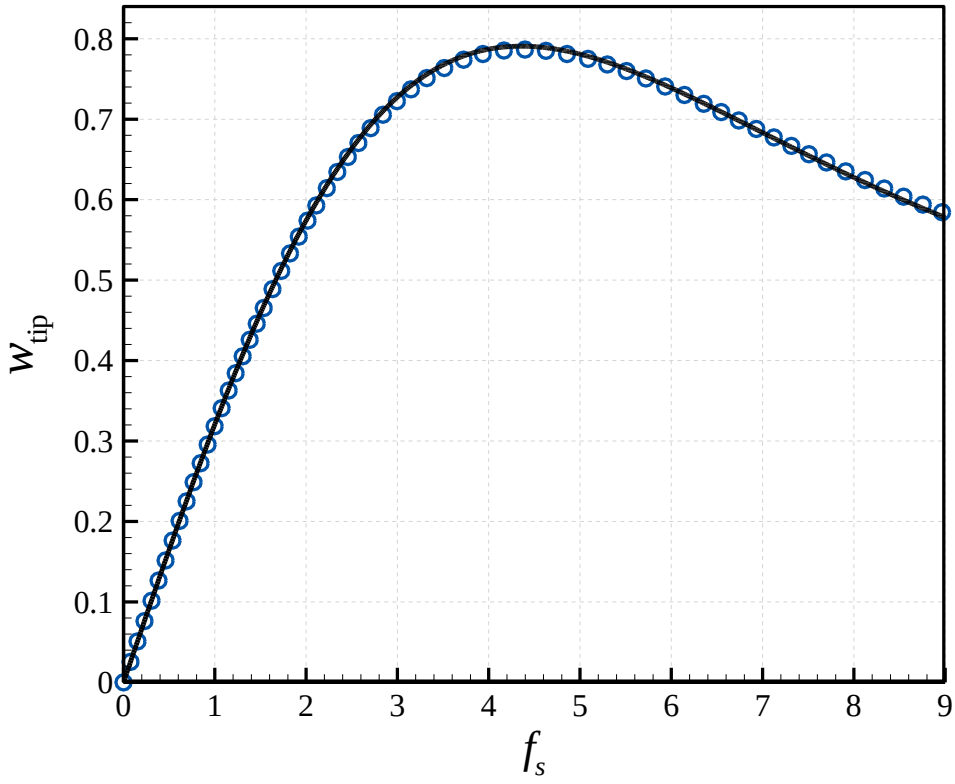

(b)

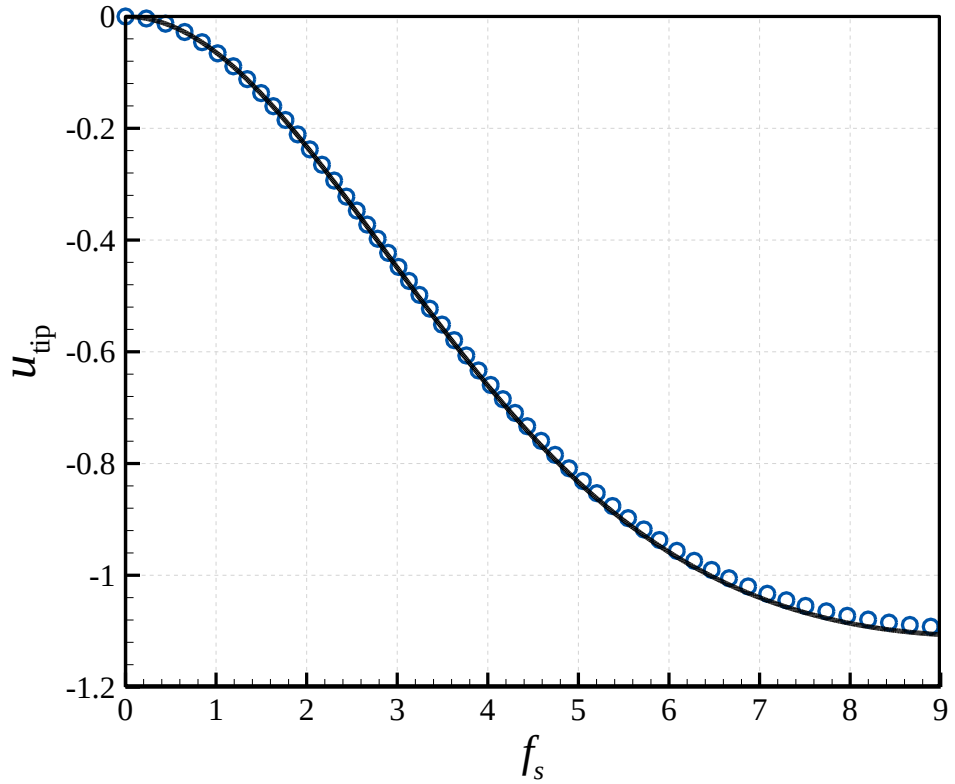

Fig.13. Comparison between the cantilever tip deflections under perpendicular tip load; (a) transverse deflection; (b) longitudinal deflection. Solid line: present study; symbols: 3D FEA.

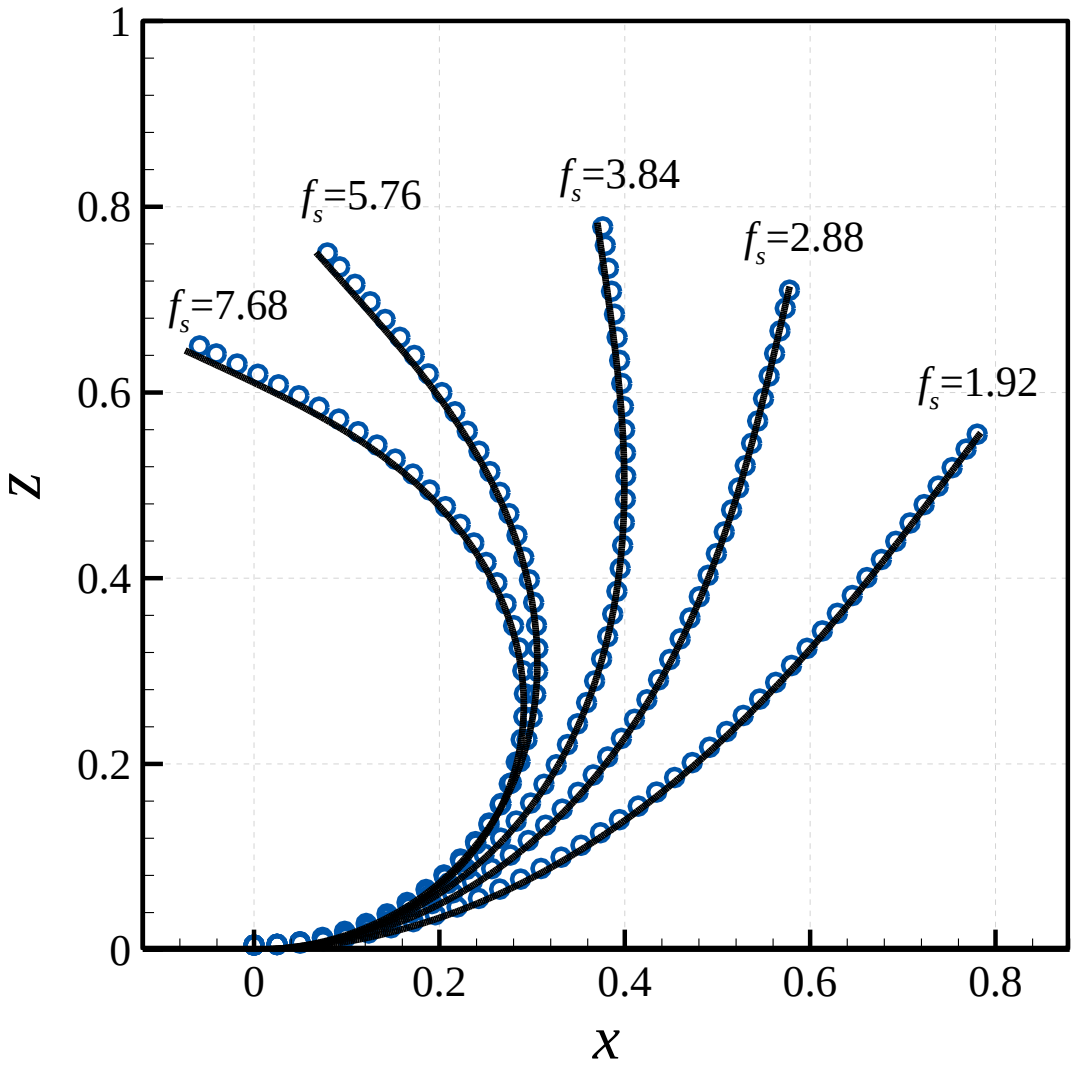

Fig.14. Deformed configuration of the cantilever at various forcing amplitudes. Solid line: present study; symbols: 3D FEA.

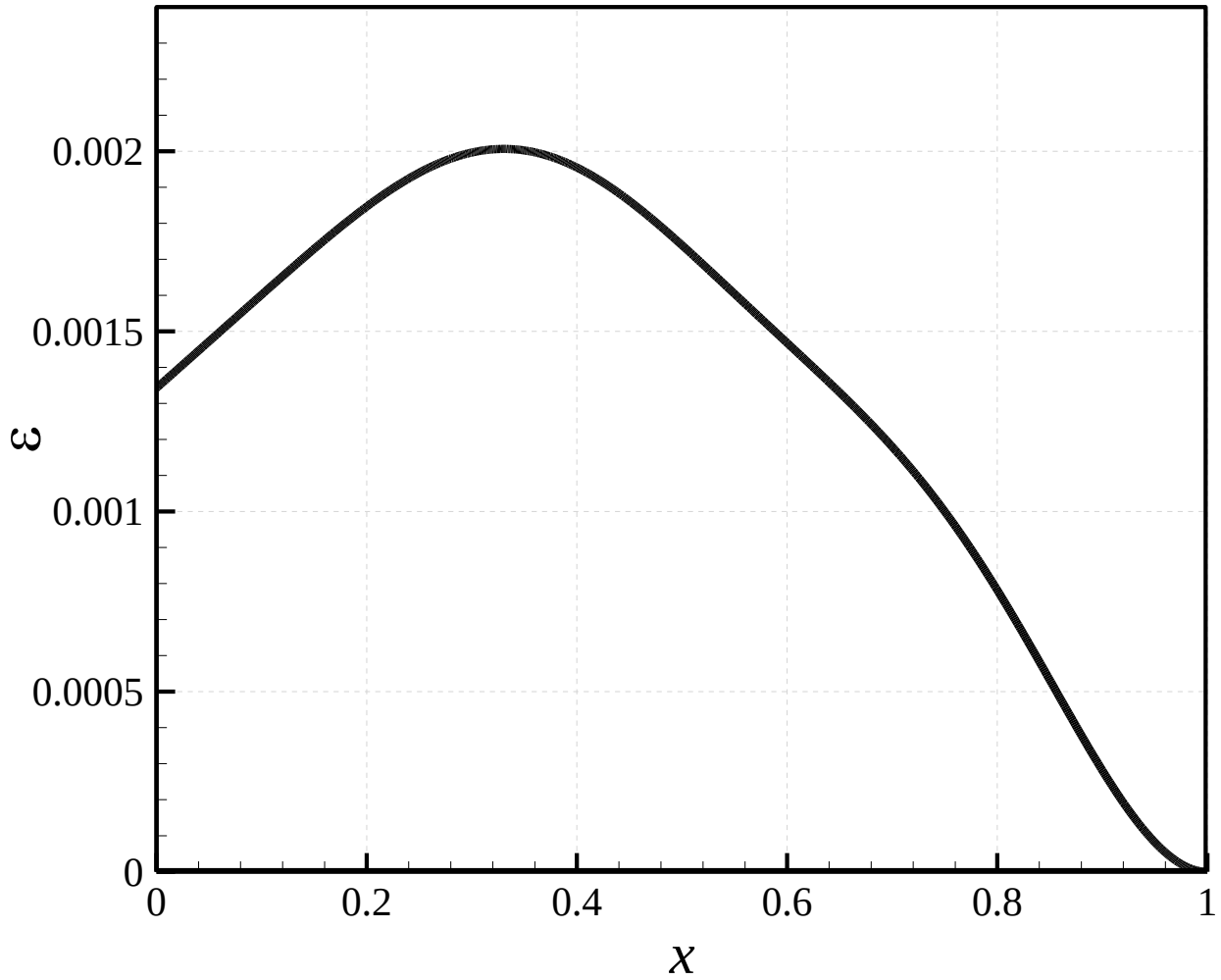

Fig.15. Strain distribution as a function of x at z = -h/2 for cantilever under static load f_s=7.68 (the case with the largest force in Fig. 14).

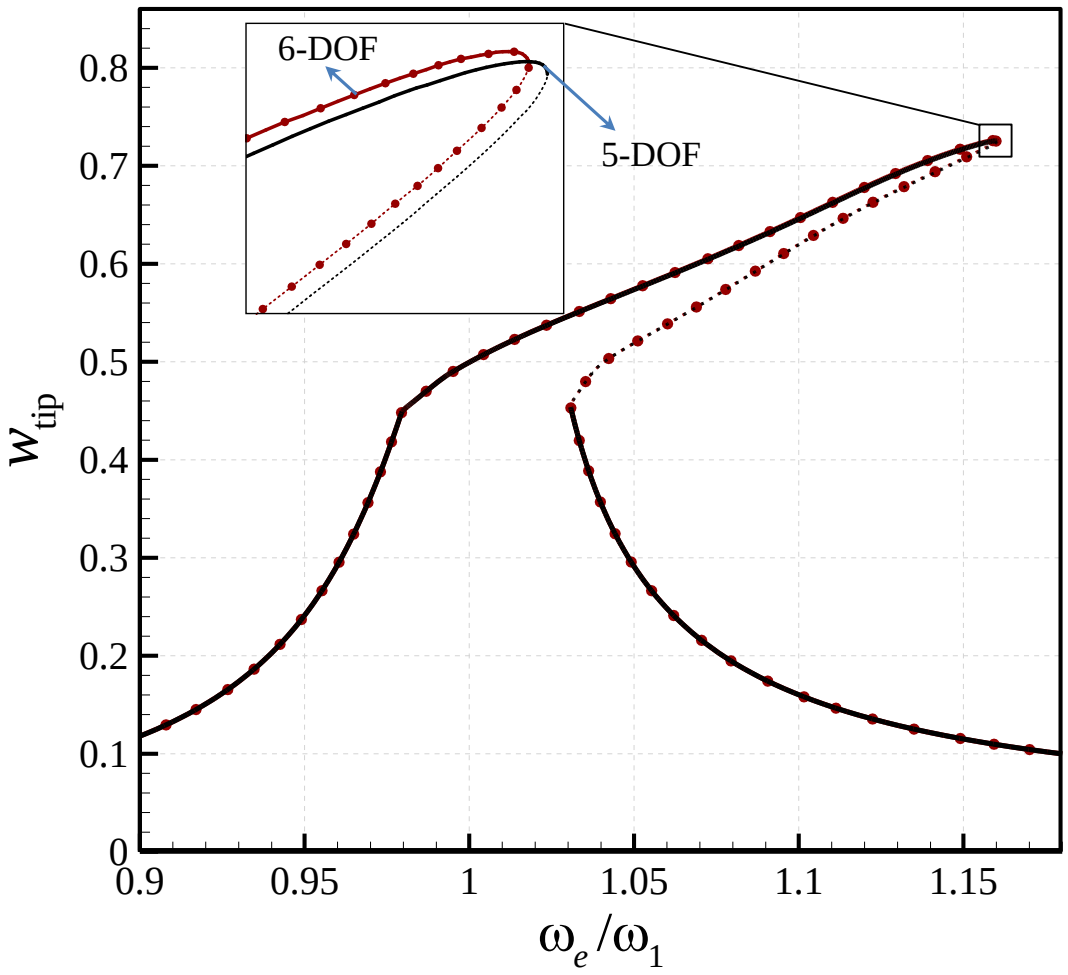

16. Effect of number of degrees of freedom on the frequency-amplitude diagrams of the system.